


 Cite this: *Nanoscale*, 2025, **17**, 8731

In vitro recording and stimulation performance of multi-electrode arrays passivated with plasma-enhanced atomic layer-deposited metal oxides†

 Yong Hee Kim,^a Jaehee Lee,^b Jung Wook Lim,^b Kukjoo Kim,^c Dae Hyun Ahn,^c Congqi Yang,^d Seongjun Park,^d Min Sun Kim^e and Sang-Don Jung^{*,a}

To achieve an intimate contact between neuronal cells and the electrode in non-invasive platforms intended for neurological research, in this study, we fabricated a raised-type Au multi-electrode array (MEA) by employing nanoscale-thick indium–tin oxide (ITO; 50 nm) as a track layer and plasma-enhanced atomic layer-deposited (PEALD) Al₂O₃ (30–60 nm) and HfO₂ (20 nm) as passivation layers. The PEALD Al₂O₃-passivated Au MEA was subsequently modified with electrodeposited AuPt nanoparticles (NPs) and IrO_x to demonstrate the passivation capability and chemical resistance of Al₂O₃ to Au-, Pt-, and IrO_x NP-containing electrolytes. Al₂O₃-passivated and IrO_x/AuPt-modified MEAs could resolve optogenetically activated spikes and spontaneous activities with a root-mean-square noise level of 2.8 ± 0.3 μV generated by the primarily cultured hippocampal neurons transfected with viral vectors. PEALD Al₂O₃ exhibited a poor resistance to the Ag leaching environment (concentrated nitric acid maintained at 70 °C); therefore, a nanoporous Au (NPG) structure could not be implemented on the Au MEA passivated with Al₂O₃. By depositing a 20 nm-thick HfO₂ over a 40 nm-thick Al₂O₃ layer, the NPG structure could be implemented on the Au MEA, confirming the chemical resistance of HfO₂ to the Ag leaching environment. The nontoxicity of Al₂O₃ and HfO₂ was confirmed by the successful primary culture of dissociated hippocampal neurons and electrophysiological studies performed using a hippocampal slice. Considering the advances in ALD technology and the vast number of metal oxides, these results extend the application of ALD metal oxides from water barriers for biomedical implants to passivation layers for *in vitro* MEAs.

Received 9th December 2024,

Accepted 8th March 2025

DOI: 10.1039/d4nr05179c

rsc.li/nanoscale

Introduction

Substrate-integrated multi-electrode arrays (MEAs) or micro-electrode arrays are *in vitro* medium-throughput extracellular or non-invasive platforms for interfacing cultured neuronal networks, electrogenic cells, acute brain slice tissues, organotypic slice cultures, and organoids.¹ Owing to their minimized

in vivo interactions, biocompatibility, non-destructive extracellular interfacing nature, and scalability, MEAs provide culture-wide field potentials, such as action potentials or spikes, and enable recording with a sub-millisecond temporal resolution, safe stimulation, and population- or network-level recording. Owing to these advantages, MEAs have been widely used to examine neurological disorders,² investigate physiological mechanisms, study learning and memory mechanisms, model neurological diseases and the brain network, and screen for drugs and neurotoxicants.³ Since earlier reports on the fabrication of MEAs,^{4–7} significant research has been conducted on technical issues related to MEAs: surface modification of the electrode with conductive nanostructured materials to reduce noise *via* impedance lowering,⁸ robust passivation,⁹ high-density electrode arrays,¹⁰ low-cost fabrication,¹¹ and 3D electrode fabrication.¹² The inefficient passivation is primarily a concern in electrode surface modification using nanostructures *via* the electrodeposition of metallic nanoparticles (NPs).

Conventionally, an MEA comprises a substrate, conductive track layer, and passivation layer. The conductive track layer

^aCybreBrain Research Section, Electronics and Telecommunications Research Institute, 218 Gajeong-ro, Yuseong-gu, Daejeon 305-700, Republic of Korea. E-mail: jungpol@etri.re.kr

^bNext-Generation Semiconductor Device Research Section, Electronics and Telecommunications Research Institute, 218 Gajeong-ro, Yuseong-gu, Daejeon 305-700, Republic of Korea

^cReality Display Research Section, Electronics and Telecommunications Research Institute, 218 Gajeong-ro, Yuseong-gu, Daejeon 305-700, Republic of Korea

^dSchool of Transdisciplinary Innovations, Seoul National University, Seoul 08826, Republic of Korea

^eDepartment of Physiology, Wonkwang University School of Medicine, 895 Munwang-ro, Iksan 570-711, Jeollabuk-do, Republic of Korea

† Electronic supplementary information (ESI) available. See DOI: <https://doi.org/10.1039/d4nr05179c>

forms the base electrodes, base reference electrode, contact pads, and tracks that electrically connect the electrodes and contact pads (see Fig. S1† for the schematic definitions of these terms). Since the incipient stage of MEA development, indium–tin oxide (ITO) has long been used as a material for the conductive track layer,^{5,6,13} owing to its unique conductive and optically transparent properties, which provide full visibility of the cultured networks from the bottom side during neuronal recording. Typically, ITO track layers thicker than 100–150 nm are used. However, ITO is seldom used as an electrode material for recording and stimulations due to its high impedance resulting from excessive polarisation and very low charge injection capability. The passivation layer is an essential element that insulates tracks and defines the active electrode region. Although polymeric materials, such as parylene,¹⁴ polyimide,⁷ polydimethylsiloxane (PDMS),¹⁵ polystyrene,¹⁶ and SU-8,¹¹ have been used as passivation layers, they lack long-term durability for repeated use.

Passivation with inorganic dielectric materials, such as silicon oxide and silicon nitride, has long been the ‘gold standard’ process^{17–21} because these materials provide sufficient insulation, robustness, and optical transparency. These dielectric layers are formed by plasma-enhanced chemical vapour deposition. However, these materials lack conformality, because of which a dielectric layer that is at least two to three times thicker than the track layer is deposited. With an increase in the thickness of the track layer, a thicker passivation layer is deposited (which requires extended dry etching), frequently damaging the electrode surface. Therefore, adopting a thinner track layer and a passivation layer with excellent conformality could help reduce the fabrication time and minimise damage to the electrode surface. In addition, a thinner passivation layer enhances the signal amplitude by reducing the distance between the electrode and the neuronal cells, given that the amplitude is inversely proportional to the square of the distance.

In this study, we fabricated MEAs using nanoscale (<100 nm) ITO and plasma-enhanced atomic layer-deposited (PEALD) metal oxides as the conductive track and passivation layers, respectively, to achieve an intimate contact between the neuronal cells and the electrode. Because PEALD enables the atomic layer deposition (ALD) of metal oxides at relatively lower temperatures (<300 °C),²² it can create the passivation layer over the ITO track layer without any thermal decomposition of ITO while preserving the merits of ALD, which are its excellent conformality, extremely low pin-hole density, and low water vapour transmission rate (WVTR) even in the presence of a very thin layer (5–100 nm). With advances in ALD technology, ALD alumina (Al₂O₃), ALD hafnium oxide (HfO₂), and their multiple stacks have been explored as moisture barriers in encapsulating the Utah electrode array,²³ polyimide-based flexible neural probe,²⁴ and biomedical implants.²⁵ An ALD HfO₂ layer has also been used as a passivation layer for planar microelectrodes²⁶ and a protecting layer for titanium nitride electrodes.²⁷ However, to the best of our knowledge, there have been no reports on the fabrication of MEAs passivated with

PEALD metal oxides nor on their recording and stimulation performance. Prior to the fabrication of the PEALD metal oxide-passivated MEA, we investigated the effect of ITO thickness on the electrode properties in terms of the impedance and charge storage capacitance (CSC) to derive the optimal ITO thickness. We also investigated the electrode surface modification capability of PEALD metal oxide-passivated Au MEAs *via* the electrodeposition of metallic NPs in terms of the impedance, CSC, and charge injection limit (CIL). We are investigating the surface modification of an Au electrode with a nanoporous Au (NPG) structure, which exhibits efficient charge injection capabilities.^{28,29} Since the formation of an NPG structure involves chemical treatment (*e.g.*, concentrated HNO₃ maintained at 70 °C), the primary concern is the chemical robustness of a nanoscale-thick PEALD metal oxide passivation layer to such a harsh chemical environment. To examine the *in vitro* neuronal recording and stimulation performance of the PEALD-passivated MEA, we recorded optogenetically excited and spontaneous spikes from viral vector-transfected hippocampal neuronal cultures and evoked local field potentials (eLFPs) from electrically stimulated hippocampal slices, respectively (see ESI Note† for the definition of eLFP).

Experimental

MEA fabrication

In this study, two types of MEAs were fabricated using passivation materials (see Fig. S2† for the schematic classification of MEAs). One type comprised ITO and Au MEAs passivated with SU-8. They were used to investigate the effect of ITO thickness on the impedance of the electrodes and the surface modification of the Au electrode *via* the electrodeposition of metallic NPs. The other type comprised ITO and raised Au MEAs passivated with PEALD metal oxides. In summary, (1) ITO MEAs passivated with 30–60 nm-thick Al₂O₃ to investigate the effect of Al₂O₃ thickness on the impedance, and (2) raised Au MEAs passivated with Al₂O₃ and Al₂O₃–HfO₂ stacks to investigate the chemical resistance.

Passivation with SU-8. A non-alkali glass (49 mm × 49 mm × 0.7 mm) sputter-coated with a 50–300 nm-thick ITO layer (AMG, Korea) was used as the starting substrate. First, the substrate was treated in a cleaning solution (SC88-500, Fischer Scientific) under sonication for 2 min; rinsed with deionised water (DIW), acetone, and methanol; and dried using N₂ gas. Standard photolithography and wet etching were performed to transfer the designed MEA layout (Fig. S1†) onto the ITO layer. After spin-coating of the positive photoresist (PR) (AZ GXR 601 46 CP, AZ Electronic Materials), the substrate was prebaked on a hot plate (100 °C for 3 min). The PR-coated substrate was exposed to an ultraviolet (UV; wavelength: 365 nm) dose of 130 mJ cm⁻² through a quartz chromium photomask. The exposed PR was developed in a developer solution (AZ 300 MIF, Merck) and then rinsed with DIW and dried using N₂ gas, followed by hard baking on a hot plate (130 °C for 10 min). ITO etching was performed by immersing the substrate in an

ITO etchant (LCE-12, Cyantek) maintained at 30 °C, followed by rinsing with DIW and drying with N₂ gas. The ITO etching time differed for different ITO thicknesses, as determined from field-emission scanning electron microscopy (FESEM) images with respect to the etching time. After ITO etching, the remaining PR was stripped twice with acetone under sonication for 5 min.

For passivation, SU-8 (SU-8 3005, Kayaku Advanced Materials) was spin-coated on the surface of the sample and prebaked on a hot plate (95 °C for 1 min 30 s). After UV exposure at a dosage of 80 mJ cm⁻², the sample was treated by a two-step post-exposure bake (PEB) on a hot plate (60 °C for 1 min and 95 °C for 2 min). To open the active electrode region, the unexposed SU-8 was removed using a developer (SU-8 Developer, Kayaku Advanced Materials), followed by washing with isopropyl alcohol, yielding SU-8-passivated ITO MEA. Although the photopatterning of SU-8 is a simple process, it remains challenging to achieve the designed fidelity with an optical waveguide structure comprising an ITO waveguide layer and two cladding layers, a glass substrate, and an SU-8 layer (Fig. S4†). The ITO waveguide layer reduces the optical intensity incident on the SU-8 layer by confining the reflected light from both the bottom glass substrate and the SU-8 layer within the ITO layer, which in turn increases the optimal exposure dose for the full crosslinking of SU-8, leading to the formation of thin crosslinked SU-8 on the ITO electrode. To solve this problem, some efforts have been made to reduce reflections by attaching an opaque film³⁰ or a light-absorbing spin-coated negative PR³¹ on the back side of the glass. In this study, a microporous vacuum chuck was used to reduce unwanted reflections.

To fabricate an SU-8-passivated Au MEA, an Au electrode was created on the ITO base electrode using the lift-off technique prior to passivation. For image reversal, PR (AZ 5214E, AZ Electronic Materials) was spin-coated onto the surface of the ITO-patterned sample and prebaked on a hot plate (110 °C for 1 min). The sample was exposed to a UV dose of 16 mJ cm⁻², followed by PEB on a hot plate (120 °C for 2 min). After subsequent UV exposure at a dose of 130 mJ cm⁻², the sample was immersed in the developer solution (AZ 300 MIF, Merck), resulting in a negative wall profile for lift-off. After the subsequent sputter deposition of a 10 nm-thick Cr and an 80 nm-thick Au, lift-off was performed by immersing the sample in acetone under sonication. The same passivation of the Au electrode with SU-8 yielded the SU-8-passivated Au MEA.

Passivation with PEALD metal oxides. Prior to PEALD metal oxide passivation, the same ITO track pattern was transferred to a 50 nm-thick ITO layer, as described in the previous section. Next, Al₂O₃ and HfO₂ layers were formed using a PEALD system (iOV D300, ISAC Research, Korea). Trimethylaluminium (iChems, Korea) and tetrakis (ethylmethylamino)hafnium(IV) (iChems, Korea) were used as precursors for Al₂O₃ and HfO₂, respectively. Ar was used as a carrier gas and for purging. O₂ gas served as a reactive source during plasma exposure, allowing the formation of high-density films at 300 °C. The thicknesses of the deposited

layers were determined using cross-sectional transmission electron microscopy (TEM). Preceded by the typical photolithographic patterning of a positive PR, the passivation layer was dry-etched to open the pads and ITO electrodes using a helical RIE system (NSE8100-0001, NEXSO, Korea). CF₄ and Ar gases were fed as reactive gases at a flow rate ratio of 4:1 and a working pressure of 5 mTorr. The etch rates determined from ellipsometry measurements (M-2000 V, J.A. Woollam) for Al₂O₃ and HfO₂ were 2.0 and 1.67 Å s⁻¹, respectively, and the dual-stacked passivation layer was etched *in situ* under identical process conditions. The removal of the dry-etched PR mask using acetone yielded a PEALD metal oxide-passivated ITO MEA with a diameter of 30 μm. To obtain the raised-type Au MEA, a 10 μm-diameter hole was created on the ITO base electrode *via* dry etching. Subsequently, a 30 μm-diameter Au electrode was created on top of the opened hole *via* radio frequency sputter deposition (20 nm-thick Cr and 80 nm-thick Au), followed by the lift-off process described in the previous section (see Fig. S3† for the schematic of the fabrication process).

Electrochemical measurements and electrode modification.

Prior to the electrochemical modification of Au MEAs, a glass ring was attached to the fabricated MEA with biocompatible-grade PDMS. All electrochemical measurements and depositions were performed using a ModuLab Femtostat system (Solartron Analytical) in a conventional three-electrode configuration,^{32,33} in which the fabricated Au MEA, Pt plate, and Ag/AgCl in a saturated KCl solution were used as the working, counter, and reference electrodes, respectively. The electrochemical properties of the electrodes were characterised in terms of the impedance, CSC, and CIL using electrochemical impedance spectroscopy (EIS), cyclic voltammetry (C-V), and transient voltage measurements, respectively. EIS data were measured at frequencies ranging from 100 kHz to 0.1 Hz at a fixed potential of 0 V. C-V curves were recorded at a sweep rate of 20 mV s⁻¹. The CSC data were estimated by integrating the cathodic part of the C-V curves. In the voltage transient measurements, the voltage transient response was induced using a biphasic cathodic-first current pulse with a pulse width of 100 μs. All the electrochemical measurements were performed in a 0.1-M KCl solution containing 1.0 mM K₄Fe(CN)₆/K₃Fe(CN)₆.

Au MEAs passivated with both SU-8 and 40 nm-thick Al₂O₃ were modified with AuPt in the potentiostatic mode with an applied voltage of -0.2 V for 10 min in a 0.5-M H₂SO₄ solution (pH = 0.3) containing 1.2 mM of H₂AuCl₄ and 3.6 mM of H₂PtCl₆. For modifying the raised-type Au MEA with nanoporous Au (NPG), an AgAu alloy was electrochemically co-deposited at -0.9 V in a 0.5-M KOH solution (pH = 13.7) containing 50 mM of K[Au(CN)₂], 50 mM of K₂Ag(CN)₃, and 0.2 M of KCN, followed by Ag leaching in concentrated HNO₃ maintained at 70 °C for 15 min, resulting in an NPG structure. All AuPt and NPG MEAs were further modified with IrO_x *via* electrodeposition in a solution (pH = 10.5; see Fig. S3† for the schematic of the Au electrode modifications *via* electrodeposition) prepared according to the procedure described by Hu

*et al.*³⁴ All the chemicals except HNO₃ (Junsei) were purchased from Sigma-Aldrich and used without further purification.

***In vitro* recording and stimulation**

Optogenetic electrophysiology. The recording performance of the IrO_x/AuPt MEA passivated with Al₂O₃ was evaluated by recording optogenetically activated spikes and spontaneous activities. For optogenetic activation, blue and yellow bottom-emitting tandem organic light-emitting devices (OLEDs) were placed on the surface of ITO-coated glass and vertically stacked with the fabricated MEA. The OLED light emission spectra were measured using a CS-2000 spectroradiometer (Konica Minolta), and the optical power density (OPD) was assessed using an integrating sphere and a photodiode (LE-5400, Otsuka Electronics). The detailed properties of the organic materials and the OLED structure have been previously reported.^{35,36}

The primary hippocampal neuronal cells dissociated from neuronal rat pups (P0) were seeded and cultured on the MEA treated with the poly-D-lysine solution (Cat# P7607, Sigma Aldrich). After 5 days of seeding, the culture was transfected with both AAV2-CaMKII α -hChR2-mCherry and AAV2-CaMKII α -ArchT3.0-eYFP (>10¹² transducing units per mL) viral vectors. After 1 week of incubation, the experiments were performed on the transfected neuronal cultures. Neuronal activity was recorded using an Intan RHS amplifier and controller (128ch RHS Stim/Recording System, Intan Technologies). The Intan RHS system was synchronised with an arbitrary waveform generator (Analog Discovery 2, Digilent) that generated the OLED driving signals (Fig. S5[†]). The sampling frequency was set to 20 kHz, and the root-mean-square (rms) noise level V_{rms} was estimated using $(\sum V_k^2/K)^{1/2}$, where V_k ($k = 1 - K$) is sampled from the $K = 20\,000$ (1.0 s) period in the signal.

***In vitro* hippocampal slice electrophysiology.** The stimulation performance of IrO_x/NPG MEAs passivated with the Al₂O₃-HfO₂ stack was evaluated by estimating the stimulation intensity or charge setting, inducing the half maximum amplitude of eLFPs in the cornu ammonis 1 (CA1) area of the hippocampus. For this, hippocampal slices were prepared using mice from the acute carbon monoxide intoxication (ACOI) ($n = 5$) and control groups ($n = 5$). The ACOI mouse model was established according to previously published protocols,³⁷ and hippocampal slices were prepared according to our previous study.³⁸ All the animal experiments were performed in strict accordance with the regulations for the Care and Use of Laboratory Animals of the National Institute of Animal Health and the Guidance by the Ethics Committee of Wonkwang University (WKU23-65). Each hippocampal slice was gently placed and immobilised on the MEA using self-made silver anchors. Slices were perfused with oxygenated artificial cerebrospinal fluid maintained at 30 °C at a rate of 2 mL min⁻¹ using an automatic temperature controller (TC-324c, Warner Instruments, Holliston, USA) and a peristaltic pump (Harvard Apparatus, Cambridge, USA). To induce eLFPs in the CA1 area, a biphasic pulse (0.1 ms, 10–90 μ A, 0.05 Hz) was applied to one electrode that was located in the stratum radiatum (SR)

layer of the CA1 area. The eLFPs were filtered (10–300 Hz) and sampled at 20 kHz using a home-built multichannel recording and stimulation system.³⁹ For each slice, the amplitude for a stimulation pulse was gradually increased from 10 to 200 μ A in increments of 20 μ A at a frequency of 0.033 Hz and a duration of 40 μ s to obtain the input/output (I/O) curve of eLFPs. The stimulation intensity that induced the half-maximum amplitude of the eLFPs was determined from the I/O curve.

To examine the long-term potentiation (LTP) induction capability of IrO_x/NPG MEAs passivated with Al₂O₃-HfO₂ stacks, LTP induction rates were compared between the two groups. Prior to LTP induction, field excitatory postsynaptic potentials with half-maximal amplitudes were recorded at 1 min intervals for 30 min. Thereafter, a patterned theta-burst stimulation (TBS) was applied to the SR layer of the CA1 area to evoke a strong synaptic potentiation of the LFPs. The TBS comprised three pulse trains administered at 20 s intervals with 10 bursts administered at 5 Hz per train and four pulses administered at 100 Hz per burst. The eLFP recording continued for 60 min after applying the TBS. After selecting four recording channels exhibiting the representative eLFP, the maximum slope of the eLFP of each channel was estimated and expressed as a percentage of the eLFP value relative to the average value of the first five baseline points from each recording channel. To compare the LTP induction rates between the groups, LTP induction rates (expressed as percentages) were collected and averaged from four recording channels per slice. The LTP induction rates were analysed in three slices from each experimental animal. Data of the LTP induction rates are expressed as mean \pm standard deviation obtained from three mice in each group. Differences between the two groups were evaluated using unpaired *t*-tests. A *P*-value of less than 0.05 was considered statistically significant.

Results and discussion

Electrochemical characterisation

Effect of ITO thickness. Prior to the characterisation of SU-8-passivated MEAs, the sheet resistance of ITO was measured using the four-point probe technique (AIT Technology, Korea), and the wet etching characteristics were observed by FESEM with respect to the thickness. SU-8 passivation was adopted because it does not cause mechanical damage to the surface of the ITO electrode. As shown in Fig. 1a, the sheet resistance of ITO exhibited an exponential decrease with increasing thickness. Furthermore, as shown in Fig. S6,[†] the thick ITO exhibited a blunt wet-etched pattern edge with a rough morphology, which is an obstacle to ALD passivation. To investigate the dependence of impedance on the ITO sheet resistance and to determine the optimal ITO thickness, a series of ITO MEAs passivated with SU-8 were fabricated by varying the ITO thickness from 25 to 300 nm. As plotted in Fig. 2b, the impedance (1 kHz) of the ITO electrodes exhibited an insignificant dependence on the ITO thickness, except for a slightly higher impedance for ITO thicknesses of less than 35 nm. This result is

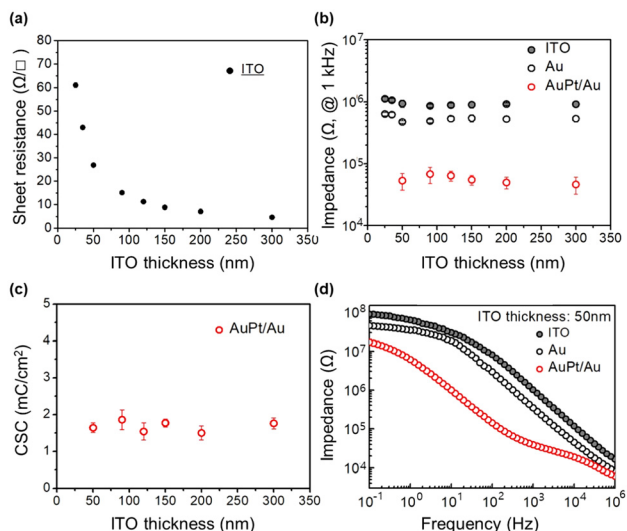


Fig. 1 (a) Sheet resistance of the adopted ITO substrates with respect to the ITO thickness. (b) Dependence of the impedance of the SU-8-passivated ITO electrode (black), Au electrode (blue), and AuPt electrode (red) on ITO thickness. (c) Dependence of the charge storage capacitance of the SU-8-passivated AuPt electrode on ITO thickness. (d) EIS results of SU-8-passivated ITO, Au, and AuPt electrodes at an ITO thickness of 50 nm.

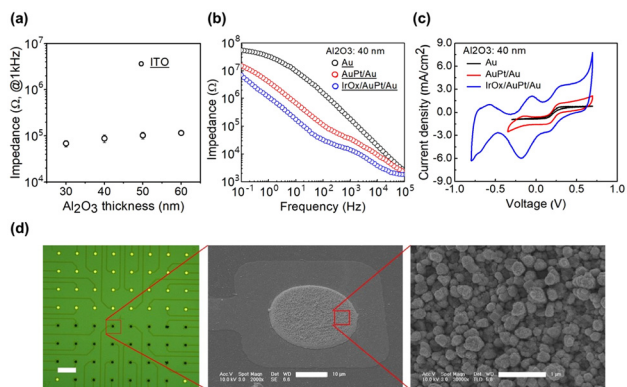


Fig. 2 (a) Al_2O_3 thickness dependence of the impedance of Al_2O_3 -passivated ITO electrode. (b) EIS results of 40 nm-thick Al_2O_3 -passivated Au-raised, AuPt, and $IrO_x/AuPt$ electrodes. (c) C-V curves of 40 nm-thick Al_2O_3 -passivated Au-raised, AuPt, and $IrO_x/AuPt$ electrodes. (d) (left) Fluorescence microscope image of the Al_2O_3 -passivated Au-raised 60-CH MEA, of which half CHs are selectively modified with AuPt. Scale bar denotes distance equal to 200 μm . (middle) FESEM image of the AuPt electrode. Scale bar denotes distance equal to 10 μm . (right) Magnified FESEM image of the morphology of the electrodeposited AuPt. Scale bar denotes distance equal to 1 μm .

consistent with that reported by Rynänen *et al.*⁴⁰ in that neither the ITO track deposition method (ion-beam assisted deposition *vs.* sputter deposition) nor the ITO sheet resistance ($2.6 \times 10^3 \Omega \square^{-1}$ *vs.* $8\text{--}10 \Omega \square^{-1}$) showed any significant difference in terms of the impedance. The capacitive impedance of the double-layer interface was orders of magnitude higher than that of the remaining recording system, including the track, which was attributed to this result.^{40,41}

To investigate the effect of track sheet resistance on the electrochemical surface modification of the Au electrode, SU-8-passivated Au MEAs were fabricated and electrochemically modified with AuPt.⁴² In the SU-8 passivation of the Au electrode, the reflection problem was significantly relieved by blocking the UV light propagating through the ITO track by the Au electrode. The impedance of the Au and AuPt electrodes exhibited an insignificant dependence on ITO thickness (Fig. 1b). The cathodic CSC of the AuPt electrode also exhibited an insignificant dependence on ITO thickness (Fig. 1c), indicating that the electrodeposition of AuPt was not significantly influenced by the sheet resistance of the ITO track layer. From the results shown in Fig. 1a–d, considering the nanoscale thickness of the PEALD passivation layer and the optical pattern contrast for alignment during photolithography, a 50 nm-thick ITO layer was selected as the optimal layer for PEALD metal oxide passivation. When the ITO thickness is less than 35 nm, it is necessary to make additional metallic alignment marks on the ITO layer due to the lack of optical pattern contrast. Hereinafter, the ITO track layer is the 50 nm-thick ITO track layer.

Al_2O_3 -passivated MEAs. Fig. 2a shows the impedance (1 kHz) of the Al_2O_3 -passivated ITO electrode with respect to the Al_2O_3 thickness. The impedance exhibited a gradually increasing tendency with increasing thickness. The impedance of the Al_2O_3 -passivated ITO electrode was one order of magnitude lower than that of the SU-8-passivated ITO electrode. This result can be attributed to the decreasing dielectric constant of Al_2O_3 with decreasing Al_2O_3 thickness.^{43,44} To examine the passivation capability of Al_2O_3 , raised-type Au MEAs were fabricated followed by subsequent modification with AuPt and IrO_x *via* electrodeposition. As shown in Fig. 2b and c, the impedance and CSC of the raised Au electrode decreased and increased, respectively, upon the subsequent electrodeposition of AuPt and IrO_x , confirming the passivation capability of Al_2O_3 . The optical microscope image showing half of the channels selectively modified with AuPt (Fig. 2d) also confirms the passivation capability of Al_2O_3 .

ALD Al_2O_3 is characterised by its low WVTR along with excellent thermal and mechanical properties²⁵ and has been used as a moisture barrier for the chronic implantation of neural electrodes.²³ However, it has poor resistance to chemical environments, such as diluted HCl and H_2SO_4 solutions (pH of 4) and acidic (1 M H_2SO_4) and alkaline solutions (1 M NaOH), but exhibits stability at a pH of 7.2 up to 168 h of exposure.⁴⁵ PEALD Al_2O_3 used in this study exhibited resistance to electrochemical solutions with a wide range of pH under the following conditions: impedance, CV measurement, AuPt NP-containing solution (pH = 0.3), and IrO_x NP-containing solution (pH = 10.5). To evaluate the chemical resistance of Al_2O_3 against harsher environments, Al_2O_3 -passivated Au MEAs were modified with NPG *via* electro-co-deposition of the Ag:Au alloy followed by the leaching of Ag in concentrated HNO_3 maintained at 70 $^\circ C$ for 15 min.^{28,46} Although the Al_2O_3 -passivated Au MEA resisted the Ag:Au containing solution, it completely dissolved following the leaching of Ag.

HfO₂-Al₂O₃ stack-passivated MEAs. To compensate for the poor chemical resistance of ALD Al₂O₃, double or triple sandwich structures with ALD HfO₂ have been applied as a moisture barrier for implantable devices.^{24,25,47} HfO₂ is known to be chemically inert, insoluble in aqueous solutions (including electrolyte environments),^{24,26} and biocompatible in terms of toxicity;²⁶ however, it has a lower WVTR than ALD Al₂O₃.⁴⁸

In this study, to investigate the chemical resistance of HfO₂ to Ag leaching (concentrated HNO₃ at 70 °C), we fabricated HfO₂ (20 nm)/Al₂O₃ (40 nm) stack-passivated raised-type Au MEAs. Fig. 3a shows the typical cross-sectional TEM images of a HfO₂ (20 nm)/Al₂O₃ (40 nm) stack deposited on a wet-etched 50 nm-thick ITO track. The figure clearly shows that the wet-etched edge of the ITO is fully covered by the PEALD layers, confirming the conformality of Al₂O₃ and HfO₂. Fig. 3b shows the fabricated Au MEA modified with NPG and IrO_x, indicating the critical role of HfO₂ in protecting Al₂O₃ in harsh Ag leaching environments. Fig. 3c and d show a decrease in the impedance and an increase in the CSC with subsequent Au surface modification with NPG and IrO_x. The roughness factor^{49,50} estimated by comparing the cathodic CSC of the Au electrode and NPG electrode was approximately 24. The CIL estimated from the voltage transient response curve (Fig. 3e) was approximately 1.6 mC cm⁻², which was lower than that (2.3 mC cm⁻²) obtained from the IrO_x/NPG-modified Au MEA fabricated using 300 nm-thick ITO and 1 μm-thick SiO₂ as the track and passivation layers, respectively.²⁹ Although the IrO_x/NPG modification conditions were not yet fully optimised, the obtained CIL was comparable to those of roughened Pt (1.0 mC cm⁻²),⁵¹ CNT (1–1.6 mC cm⁻²),⁵² and PtIr-CF (1.25 mC cm⁻²).⁵³

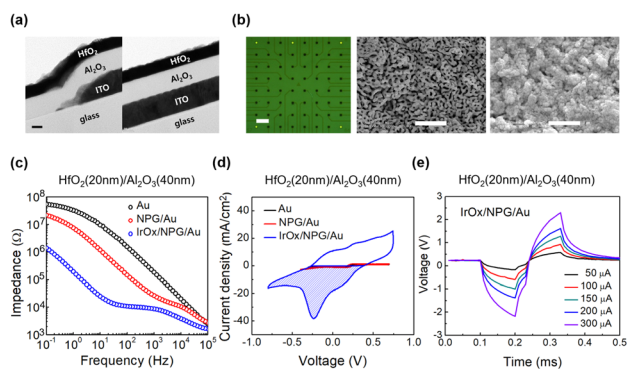


Fig. 3 (a) Typical cross-sectional TEM image of HfO₂ (20 nm)/Al₂O₃ (40 nm) stack-deposited on a wet-etched 50 nm-thick ITO track line (left: wet-etched edge; right: inner position). Scale bar denotes distance equal to 20 nm. (b) (left) Optical microscopic image of the passivated raised Au MEA modified with the NPG structure. Scale bar denotes distance equal to 200 μm. (middle) FESEM image of magnified and (right) IrO_x-electrodeposited NPG structures. Scale bars denote distance equal to 1 μm. (c) EIS results of Au, NPG, and IrO_x/NPG electrodes. (d) C–V curves of Au, NPG, and IrO_x/NPG electrodes. (e) Voltage transient response of the IrO_x/NPG electrode measured with an increasing biphasic pulse amplitude (100 μs duration and 30 μs interpulse delay).

In vitro recording performance of PEALD Al₂O₃-passivated MEAs

To evaluate the recording performance of the fabricated MEAs, blue and yellow OLEDs were integrated with Al₂O₃-passivated and IrO_x/AuPt-modified MEAs for *in vitro* optogenetic and neuronal activity recordings (Fig. 4a). Tandem-structured blue and yellow OLEDs were fabricated to achieve a high OPD (Fig. S5†), which is a critical factor for the effective optogenetic stimulation of neurons. Fig. 4b shows hippocampal neuronal

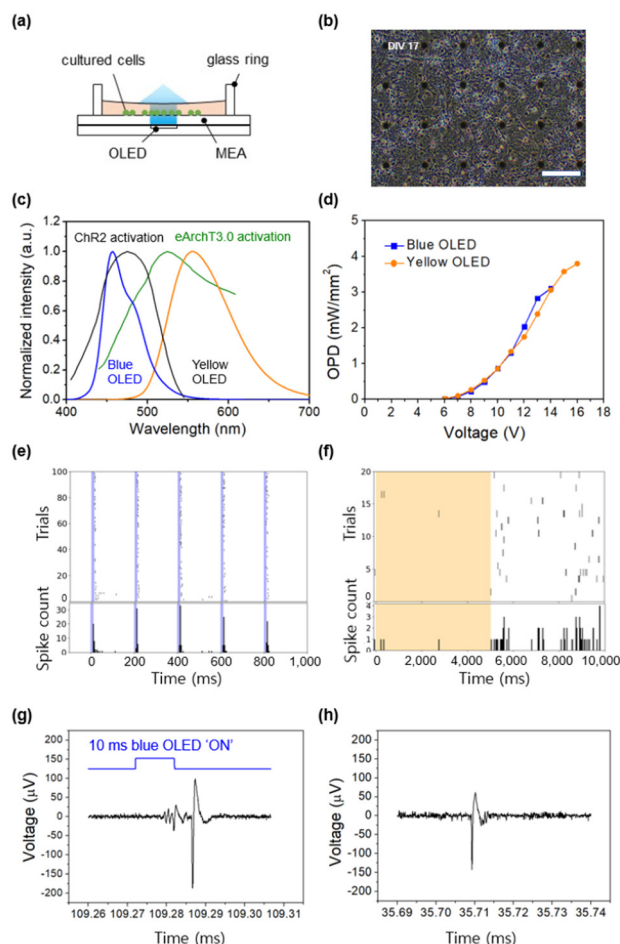


Fig. 4 Optogenetic stimulation and MEA recording: (a) schematic of the MEA–OLED integrated experimental setup. (b) Optical microscopic image of hippocampal neuronal cells cultured on a Al₂O₃-passivated AuPt MEA taken at 17 days *in vitro*. Scale bar denotes 200 μm. (c) Emission spectra of blue and yellow OLEDs and the activation spectra of archaerhodopsin (eArchT3.0; spectrum modified from ref. 51) and channelrhodopsin-2 (ChR2; spectrum modified from ref. 52). (d) OPDs of blue and yellow OLEDs. (e) Raster plot and peri-stimulus time histogram (PSTH) of the neuronal activity upon stimulation by the blue OLED. The blue-shaded region indicates OLED light stimulation, with an OPD of approximately 0.8 mW mm⁻² and a pulse width of 10 ms. The PSTH bin size is 4 ms. (f) Raster plot and PSTH of the neuronal activity upon stimulation by the yellow OLED. The orange-shaded region indicates the period of OLED light stimulation, with an OPD of approximately 2.4 mW mm⁻² and a pulse duration of 5 s. The PSTH bin size is 40 ms. (g and h) Typical spike waveforms of the optogenetically excited neuronal activity (g) and spontaneous neuronal activity (h).

cells cultured on the Al_2O_3 -passivated AuPt MEA (17 days *in vitro*), indicating non-toxicity of Al_2O_3 passivation layer. For optogenetic excitation, a blue OLED was integrated with an MEA cultured with Channelrhodopsin-2 (ChR2)-expressing neurons for optogenetic excitation, whereas a yellow OLED was paired with an MEA cultured with archaerhodopsin (eArchT3.0)-expressing neurons for optogenetic inhibition. Prior to optogenetic stimulation, the performance of the OLEDs was characterised in terms of their emission spectrum and OPD, both of which are essential for optogenetic stimulation. Fig. 4c shows the emission spectrum of the blue OLED along with the activation spectrum of ChR2. The blue OLED exhibited peak emission at approximately 457 nm with a shoulder at approximately 480 nm. This spectrum closely aligned with the activation spectrum of ChR2, which peaks at approximately 470 nm with a broad range.⁵⁴ Fig. 4c also shows the emission spectrum of the yellow OLED and the activation spectrum of eArchT3.0. The yellow OLED exhibited a peak emission at approximately 556 nm, exhibiting good alignment with that of the eArchT3.0 activation spectrum and peaking at approximately 520 nm with a broad range.^{56,57} Fig. 4d shows the measured OPD for both blue and yellow OLEDs. The blue OLED achieved a maximum OPD of approximately 3.1 mW mm^{-2} , sufficient for ChR2 activation, whereas the yellow OLED reached a maximum OPD of approximately 3.8 mW mm^{-2} , which is adequate for eArchT3.0 activation.⁵⁵

Fig. 4e and f show the raster plots and peri-stimulus time histograms (PSTHs) of the neuronal activity upon light stimulation from the blue and yellow OLEDs, respectively. To activate ChR2, the blue OLED was driven with a pulse train of 10 ms, with 200 ms intervals between each pulse. The OPD of the blue OLED was set to approximately 0.8 mW mm^{-2} with a driving voltage of 10 V. The raster plot and PSTH shown in Fig. 4e clearly demonstrate that most spikes occur immediately following blue light stimulation, with a delay of a few milliseconds, confirming successful stimulation by the OLED without optically induced artefacts. Spontaneous spikes were observed at the beginning of the experiment (trials 1–7) but diminished in later trials, presumably due to the lack of nearby ions and neurotransmitters caused by repeated optogenetic stimulation. For neural inhibition, the yellow OLED was turned on and off at 5 s intervals. The OPD of the yellow OLED was set to approximately 2.4 mW mm^{-2} with a driving voltage of 13 V. The raster plot and PSTH shown in Fig. 4f indicate suppressed neuronal activity when the yellow OLED is on; however, firing resumed when the OLED is off, confirming that yellow light effectively inhibits neuronal firing. As shown in Fig. 4g and h, the fabricated MEAs clearly resolved both optogenetically evoked and spontaneous single spikes. The optogenetically evoked spike exhibited a delay ($\sim 15 \text{ ms}$) after the light was turned on and demonstrated some ripples before spiking. A noise level V_{rms} of $2.8 \pm 0.3 \mu\text{V}$ ($N = 4$, where N indicates the number of MEAs) estimated in the quiescent state without spikes confirmed the surface modification capability of the Al_2O_3 -passivated electrode *via* the electrodeposition of metallic nanoparticles. The successful primary cultures of dis-

sociated hippocampal neurons and recordings of spikes have confirmed the biocompatibility of Al_2O_3 ^{57,58} and demonstrated that Al_2O_3 exhibits sufficient hydrolytic resistance in culture media.

Evoking *in vitro* hippocampal response

To evaluate the electrical stimulation performance of the fabricated MEAs, the hippocampal LTP-induction capability of the $\text{HfO}_2/\text{Al}_2\text{O}_3$ stack-passivated IrO_x/NPG MEA was examined using mice from the ACOI group. As shown in Fig. 5a, when a single square pulse was applied to a stimulation electrode on the SR layer, eLFPs with peak latencies of at least 5 ms were observed from five to seven electrodes in the hippocampal region. The shapes of the eLFPs varied with the position of the recording electrodes, probably because of changes in the current sink and source of pyramidal neurons activated by electrical stimulation. With an increase in the stimulation intensity, the individual slopes of the eLFPs increased and became saturated at higher current intensities, resulting in a sigmoidal distribution of the I/O curve. In the I/O curve, the current intensity range for their half-maximal response was $60\text{--}80 \mu\text{A}$ with a pulse width of $40 \mu\text{s}$ ($2.4\text{--}3.2 \text{ nC}$ per pulse). This charge setting is lower than the 3D Pt electrode ($>10.8 \text{ nC}$ per pulse)⁵⁹ and slightly higher than the Pt black electrode (2 nC per pulse)⁷ used in similar experiments. Recently, we fabri-

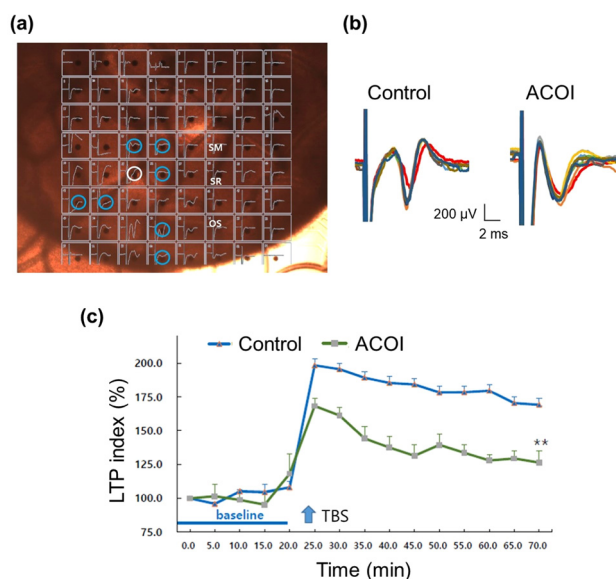


Fig. 5 Recording of eLFPs from the CA1 area of the hippocampal slice: (a) image of the mouse hippocampal slice on the MEA overlapped with corresponding channel windows representing evoked responses following single pulse stimulation to the SR layer through the electrode marked in white. The blue circles denote the recording electrode selected according to the response. (b) Changes in the representative traces of eLFPs of the control and ACOI groups following theta burst stimulation. (c) Line diagram showing changes in the induction rate of the LTP between the control and ACOI groups. A significant difference is observed in LTP induction between the control and ACOI groups ($p < 0.01$). LTP index = (slope of eLFPs at 60 min per slope of eLFPs at baseline) \times 100.

cated a photo-crosslinkable fluoropolymer-passivated flexible neural probe and achieved a CIL of 5.18 mC cm^{-2} by implementing the IrO_x/NPG structure. By performing *in vivo* micro-stimulation of Schaffer collateral fibres, we could record the evoked field excitatory postsynaptic potentials at a current intensity of $80\text{--}90 \text{ }\mu\text{A}$ and a pulse width of $40 \text{ }\mu\text{s}$ ($3.2\text{--}3.6 \text{ nC}$ per pulse).⁴⁶ Although a direct comparison of *in vivo* and *in vitro* micro-stimulations is impractical, the evoking capability under comparably low charge settings would support the micro-stimulation performance of the $\text{HfO}_2/\text{Al}_2\text{O}_3$ stack-passivated IrO_x/NPG MEA.

In the control group without COI, the TBS episodes delivered to the SR layer through a stimulation electrode resulted in a prominent increase in the eLFP slope immediately following the TBS episode. Thereafter, there was continuous upregulation of the LPF slope, with a slight decrease up to 60 min after the stimulation, indicating the occurrence of LTP (Fig. 5c). TBS reliably produced a $179.6 \pm 4.7\%$ increase in the LTP slope relative to the baseline based on the recordings for 60 min after a TBS episode, even though the induction rate of the LTP varied among the recording electrodes. In the hippocampal slice obtained from the ACOI group, there was a lower induction of LTP induced by the TBS episode compared with those of the control group, in which the induction rate of LTP was $127.8 \pm 4.5\%$ 60 min after the TBS episode, which is significantly lower than that of the control group ($p < 0.05$). This result indicates that the $\text{HfO}_2/\text{Al}_2\text{O}_3$ stack-passivated IrO_x/NPG MEA has a sufficient LTP induction capability for LTP-based hippocampal electrophysiological studies.

Conclusions

In this study, we demonstrated the fabrication of a raised-type Au MEA by employing nanoscale-thick ITO as the track layer and Al_2O_3 and HfO_2 as the passivation layers. The SU-8 passivation of the ITO track layer with a thickness ranging from 25 to 300 nm confirmed that the impedance of the ITO electrode was insensitive to the ITO thickness. Moreover, the impedance of the SU-8-passivated Au electrode and AuPt NP-modified Au electrode *via* electrodeposition exhibited an insignificant dependence on the ITO thickness, indicating that the electrode deposition of AuPt NPs was not significantly influenced by the ITO thickness. Au MEAs were fabricated by employing a nanoscale-thick ITO (50 nm) as the track layer and nanoscale-thick PEALD Al_2O_3 (30–60 nm) and HfO_2 (20 nm) as the passivation layers. The PEALD Al_2O_3 -passivated Au MEAs were subsequently modified with electrodeposited AuPt and IrO_x to demonstrate the passivation capability and chemical resistance of Al_2O_3 to Au NP-, Pt NP-, and IrO_x NP-containing electrolytes. The IrO_x/AuPt MEAs could resolve optogenetically excited spikes and spontaneous activities of cultured hippocampal neurons with an RMS noise level of $2.8 \pm 0.3 \text{ }\mu\text{V}$, confirming the recording performance of the fabricated MEA. Al_2O_3 exhibited poor resistance to the Ag leaching environment; therefore, NPG could not be implemented on the Al_2O_3 -

passivated Au electrode. However, by introducing a 20 nm-thick HfO_2 as an additional passivation layer over the 40 nm-thick Al_2O_3 layer, NPG could be implemented on the Au electrode, confirming the chemical resistance of HfO_2 to the Ag leaching environment. The IrO_x -modified NPG MEA scored a CIL of 1.6 mC cm^{-2} and evoked a half-maximal response of LFP from the CA1 area of the hippocampal slice in a low stimulation charge setting ($2.4\text{--}3.2 \text{ nC}$ per pulse). In addition, the IrO_x/NPG MEA induced LTP with a sufficient induction rate to distinguish hippocampal slices between the ACOI and control groups. The nontoxicity of Al_2O_3 and HfO_2 was confirmed by the successful primary culture of dissociated hippocampal neurons and electrophysiological studies performed using a hippocampal slice. The excellent conformality of PEALD metal oxides combined with their biocompatibility and chemical stability would help establish themselves as an efficient nanoscale passivation layer for *in vitro* MEA.

Author contributions

The manuscript was written through the contributions of all authors. Y. H. K.: investigation, methodology, and writing. J. L.: investigation. J. W. L.: methodology and review. K. K.: investigation and conceptualization. D. H. A.: investigation. C. Y.: methodology and writing. S. P.: conceptualization. M. S. K.: investigation, methodology, and writing. S.-D. J.: investigation, methodology, writing and review.

Data availability

The data supporting the findings of this study are available from the corresponding author upon reasonable request.

Conflicts of interest

The authors declare no competing financial interests or personal relationships that may have influenced the research conducted in this study.

Acknowledgements

This work was supported by Electronics and Telecommunications Research Institute grants funded by the Korean Government [grant numbers: 24ZB1330 and 24RB1310]. We would like to thank Editage (<https://www.editage.co.kr>) for English language editing.

References

- 1 A. Tanwar, H. A. Gandhi, D. Kushwaha and J. Bhattacharya, *Mater. Today Chem.*, 2022, **26**, 101153.

- 2 S. Schulte, M. Gries, A. Christmann and K.-H. Schäfer, *Bioelectron. Med.*, 2021, **7**, 15.
- 3 M. Cerina, M. C. Piastra and M. Frega, *Prog. Biomed. Eng.*, 2023, **5**, 032002.
- 4 J. Pine, *J. Neurosci. Methods*, 1980, **2**, 19–31.
- 5 G. W. Gross, W. Y. Wen and J. W. Lin, *J. Neurosci. Methods*, 1985, **15**, 243–252.
- 6 Y. Jimbo and A. Kawana, *Bioelectrochem. Bioenerg.*, 1992, **29**, 193–204.
- 7 H. Oka, K. Shimono, R. Ogawa, H. Sugihara and M. Taketani, *J. Neurosci. Methods*, 1999, **93**, 61–67.
- 8 Y. Liu, S. Xu, Y. Yang, K. Zhang, E. He, W. Liang, J. Luo, Y. Wu and X. Cai, *Microsyst. Nanoeng.*, 2023, **9**, 13.
- 9 S.-H. Ahn, J. Jeong and S. J. Kim, *Micromachines*, 2019, **10**, 508.
- 10 I. Suzuki, N. Matsuda, X. Han, S. Noji, M. Shibata, N. Nagafuku and Y. Ishibashi, *Adv. Sci.*, 2023, **10**, 2207732.
- 11 T. Ahmadvand, S. Mirsadeghi, F. Shanehsazzadeh, S. Kiani and M. Fardmanesh, *Proceedings*, 2020, **60**, 51.
- 12 J. S. Choi, H. J. Lee, S. Rajaraman and D.-H. Kim, *Biosens. Bioelectron.*, 2021, **171**, 112687.
- 13 M. Meister, J. Pine and D. A. Baylor, *J. Neurosci. Methods*, 1994, **51**, 95–106.
- 14 H. Charkhkar, D. E. Arreaga-Salas, T. Tran, A. Hammack, W. E. Voit, J. J. Pancrazio and B. E. Gnade, *Sens. Actuators, B*, 2016, **226**, 232–238.
- 15 Y. Nam, K. Musick and B. C. Wheeler, *Biomed. Microdevices*, 2006, **8**, 375–381.
- 16 A. Hammack, R. T. Rihani, B. J. Black, J. J. Pancrazio and B. E. Gnade, *Biomed. Microdevices*, 2018, **20**, 48.
- 17 P. Connolly, P. Clark, A. S. G. Curtis, J. A. T. Dow and C. D. W. Wilkinson, *Biosens. Bioelectron.*, 1990, **5**, 223–234.
- 18 U. Egert, B. Schlosshauer, S. Fennrich, W. Nisch, M. Fejtl, T. Knott, T. Muller and H. Hammerle, *Brain Res. Protoc.*, 1998, **2**, 229–242.
- 19 T. Gabay, M. Ben-David, I. Kalifa, R. Sorkin, Z. R. Abrams, E. Ben-Jacob and Y. Hanein, *Nanotechnology*, 2007, **18**, 035201.
- 20 A. Czeschik, A. Offenhausser and B. Wolfrum, *Phys. Status Solidi A*, 2014, **211**, 1462–1466.
- 21 E. He, S. Xu, G. Xiao, Y. Dai, X. Li, Y. Song, F. Gao, Y. Zhang, S. Xu and X. Cai, *Sens. Actuators, B*, 2021, **329**, 129190.
- 22 S. E. Potts, W. Keuning, E. Langereis, G. Dingemans, M. C. M. van de Sanden and W. M. M. Kessels, *J. Electrochem. Soc.*, 2010, **157**, 66–74.
- 23 X. Xie, L. Rieth, L. Williams, S. Negi, R. Bhandari, R. Caldwell, R. Sharma, P. Tathireddy and F. Solzbacher, *J. Neural Eng.*, 2014, **11**, 026016.
- 24 L. Merken, M. Schelles, F. Ceysens, M. Kraft and P. Janssen, *J. Neural Eng.*, 2022, **19**, 066039.
- 25 C. Li, M. Cauwe, Y. Yang, D. Schaubroeck, L. Mader and M. O. de Beeck, *Coatings*, 2019, **9**, 579.
- 26 J. L. Collins, H. M. Hernandez, S. Habibi, C. E. Kendrick, Z. Wang, N. Bihari, P. L. Bergstrom and A. R. Minerick, *Thin Solid Films*, 2018, **662**, 60–69.
- 27 M. Dollt, M. Reh, M. Metzger, G. Heusel, M. Kriebel, V. Bucher and G. Zeck, *Front. Neurosci.*, 2020, **14**, 552876.
- 28 Y. H. Kim, G. H. Kim, A. Young, Y. H. Han, M.-A. Chung and S.-D. Jung, *J. Neural Eng.*, 2015, **12**, 066029.
- 29 Y. H. Kim, G. H. Kim, M. S. Kim and S.-D. Jung, *Nano Lett.*, 2016, **16**, 7163–7168.
- 30 I. A. Weaver, A. W. Li, B. C. Shields and M. R. Tadross, *J. Neural Eng.*, 2022, **19**, 024001.
- 31 H. S. Jeong, S. Hwang, K. S. Min and S. B. Jun, *Micromachines*, 2021, **12**, 1347.
- 32 A. C. Lazanas and M. I. Prodromidis, *ACS Meas. Sci. Au*, 2023, **3**, 162–193.
- 33 S. Cui, F. Wang and W. Yang, *Sens. Actuators, B*, 2025, **425**, 136996.
- 34 J. Hu, M. Abdelsalam, P. Bartlett, R. Cole, Y. Sugawara, J. Baumberg, S. Mahajan and G. Denuault, *J. Mater. Chem.*, 2009, **19**, 3855–3858.
- 35 J. Park, J.-H. Lee, J. Lee and H. Cho, *J. Inf. Disp.*, 2021, **22**, 107–113.
- 36 H. Cho, C. W. Joo, S. Choi, C. Kang, G. H. Kim, J.-W. Shin, B.-H. Kwon, H. Lee, C.-W. Byun and N. S. Cho, *ETRI J.*, 2021, **43**, 1093–1102.
- 37 S. T. Kim and S. J. Yoo, *J. Korean Soc. Clin. Toxicol.*, 2021, **19**, 100–109.
- 38 G. W. Lee, J. H. Kim and M. S. Kim, *Korean J. Physiol. Pharmacol.*, 2017, **21**, 423–428.
- 39 J. Park, G. Kim and S.-D. Jung, *IEEE Trans. Neural Syst. Rehabil. Eng.*, 2017, **25**, 2227–2237.
- 40 T. Ryyänen, R. Mzezewa, E. Meriläinen, T. Hyvärinen, J. Lekkala, S. Narkilahti and P. Kallio, *Micromachines*, 2020, **11**, 497.
- 41 A. Blau, *Curr. Opin. Colloid Interface Sci.*, 2013, **18**, 481–492.
- 42 Y. H. Kim, A. Y. Kim, G. H. Kim, Y. H. Han, M.-A. Chung and S.-D. Jung, *Biomed. Microdevices*, 2016, **18**, 14.
- 43 M. D. Groner, J. W. Elam, F. H. Fabreguette and S. M. George, *Thin Solid Films*, 2002, **413**, 186–197.
- 44 Y. Etinger-Geller, E. Zoubenko, M. Baskin, L. Kornblum and B. Pokroy, *J. Appl. Phys.*, 2019, **125**, 185302.
- 45 H. Krýsová, M. Neumann-Spallart, H. Tarábková, P. Janda, L. Kavan and J. Krýsa, *Beilstein J. Nanotechnol.*, 2021, **12**, 24–34.
- 46 Y. H. Kim, H. Koo, M. S. Kim and S.-D. Jung, *Biomater. Adv.*, 2023, **154**, 213629.
- 47 T. Kono, Y. Terasawa, H. Tashiro, T. Ueno and J. Ohta, *Sens. Mater.*, 2022, **34**, 1577–1586.
- 48 L. H. Kim, J. H. Jang, Y. J. Jeong, K. Kim, Y. Baek, H.-J. Kwon, T. K. An, S. Nam, S. H. Kim, J. Jang and C. E. Park, *Org. Electron.*, 2017, **50**, 296–303.
- 49 M. D. Scanlon, U. Salaj-Kosla, S. Belochapkin, D. MacAodha, D. Leech, Y. Ding and E. Magner, *Langmuir*, 2012, **28**, 2251–2261.
- 50 X. Xiao, P. Si and E. Magner, *Bioelectrochemistry*, 2016, **109**, 117–126.
- 51 A. Weremfo, P. Carter, D. B. Hibbert and C. Zhao, *Langmuir*, 2015, **31**, 2593–2599.

- 52 K. Wang, H. A. Fishman, H. Dai and J. S. Harris, *Nano Lett.*, 2006, **6**, 2043–2048.
- 53 E. della Valle, E. J. Welle, C. A. Chestek and J. D. Weiland, *J. Neural Eng.*, 2021, **18**, 054001.
- 54 M. L. Rein and J. M. Deussing, *Mol. Genet. Genomics*, 2012, **287**, 95–109.
- 55 J. Mattis, K. M. Tye, E. A. Ferenczi, C. Ramakrishnan, D. J. O'Shea, R. Prakash, L. A. Gunaydin, M. Hyun, L. E. Fenno, V. Gradinaru, O. Yizhar and K. Deisseroth, *Nat. Methods*, 2012, **9**, 159–172.
- 56 Z. C. Wick and E. Krook-Magnuson, *Front. Cell. Neurosci.*, 2018, **12**, 151.
- 57 D. S. Finch, T. Oreskovic, K. Ramadurai, C. F. Herrmann, S. M. George and R. L. Mahajan, *J. Biomed. Mater. Res., Part A*, 2007, **87**, 1–282.
- 58 I. Spajić, M. G. Morais, C. Monteiro, M. Cristina, L. Martins, A. P. Pêgo and I. Milošev, *J. Mater. Sci.: Mater. Med.*, 2024, **35**, 68.
- 59 M. O. Heuschkel, M. Fejtl, M. Raggenbass, D. Bertrand and P. Renaud, *J. Neurosci. Methods*, 2002, **114**, 135–148.